THEORETICAL FRAUNHOFER LIGHT DIFFRACTION PATTERNS CALCULATED FROM THREE-DIMENSIONAL SARCOMERE ARRAYS IMAGED FROM ISOLATED CARDIAC CELLS AT REST

KENNETH P. ROOS AND ALFRED F. LEUNG
Department of Physiology and the American Heart Association Greater Los Angeles Affiliate Cardiovascular Research Laboratory, University of California, Los Angeles, California 90024-1760; and Department of Physics, The Chinese University of Hong Kong, Hong Kong

ABSTRACT Sarcomere striation positions have been obtained throughout the volumes of calcium-tolerant resting heart cells by direct computer interfaced high-resolution optical imaging. Each sarcomere position is stored in a three-dimensional (3-D) matrix array from which Fraunhofer light diffraction patterns have been calculated using numerical methods based on Fourier transforms. Diffraction patterns have been calculated from heart cell data arrays oriented normal to a theoretical laser beam. Twelve characteristic features have been identified and described from these diffraction patterns that correlate to diffraction phenomena observed from both cardiac and skeletal muscle. This numerical approach provides the means to directly assess diffraction pattern formulation, the precision of layer line angular separation, layer-line intensity and angular asymmetries, line widths and fine structures in terms of the known diffracting source structures. These results confirm that theoretical calculations can predict real muscle diffraction patterns and their asymmetries.

INTRODUCTION

During the past decade, light diffraction techniques have been widely used to measure average sarcomere length periodicity from striated muscle (1–38). The alternating A- and I-bands of striated muscle sarcomeres have differential refractive indices due to the different protein concentration of their interdigitating thick and thin filaments. Thus, if transilluminated with a monochromatic light source, such as a laser, these three-dimensional (3-D) arrays of regularly spaced sarcomeres within a muscle will exhibit a classical diffraction pattern. This pattern consists of meridional layer lines oriented perpendicular to the muscle fiber's longitudinal axis and parallel to the striation direction (Fig. 1). The spacing between the layer line orders is inversely proportional to the average sarcomere periodicity in accordance with the plane grating equation:

$$n\lambda = d \sin \alpha, \qquad (1)$$

where n is the order of the layer line (0, ±1, ±2, etc.), λ (lambda) is the wavelength of incident light (632.8 nm if from a HeNe laser), d is the average sarcomere periodicity, and α (alpha) the angle of diffraction. In addition to average sarcomere length periodicity information, investigators have also attempted to interpret data from diffraction pattern layer line intensities (2, 3, 5–10, 12, 13, 16–19, 22–24, 26, 27, 30–32, 34, 36, 37), angular positions (1, 2, 4, 5, 9–19, 22–28, 29–33, 34, 36, 37), and fine structure (1, 4, 5, 9, 12, 14, 16–19, 22–26, 29–33, 37) to address questions of sarcomere uniformity, distribution, and dynamics. It is tempting to use light diffractometry techniques to determine dynamic physical changes on a submicroscopic scale in a muscle system since any alterations in periodicity, position, or refractive index from within the illuminated region will be seen in the observed pattern. Unfortunately, this has, at times, led to conflicting results (1, 11, 28–30, 33). Thus, if one is to unambiguously derive and interpret information from diffraction patterns, the source and interaction of light scattering within the 3-D, A-and I-band sarcomere array must be understood.

Though the direct relationship between sarcomere length periodicity and meridional light diffraction layer line spacing was recognized by Ranvier (42) over a century ago, the direct correlation between sarcomeric periodicity and order to other observed diffraction phenomenon has been elusive. During the past decade, several theories based on both single and multidimensional analyses of the plane grating equation have been proposed in an attempt to address this relationship (2–4, 6–8, 12, 16, 18, 22, 24, 30, 31, 34, 36, 37). All of these theoretical approaches assume some idealized sarcomere scattering array (e.g., random ordering, skew or Bragg planes) to link their predictions to real diffraction pattern observations. To date, these assumed sarcomere distributions have not completely

BIOPHYS. J. © Biophysical Society · 0006-3495/87/08/329/13 $2.00
Volume 52 August 1987 329–341

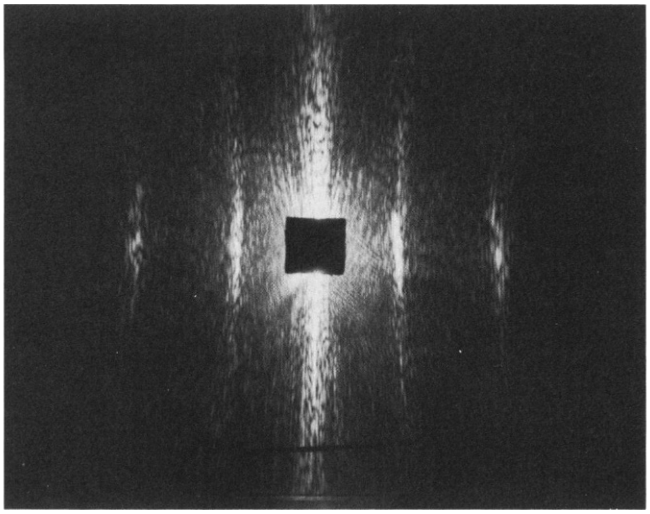

FIGURE 1 Diffraction pattern of isolated heart cell. This direct photograph illustrates the zero, first, and second order meridional layer lines. The blocked out area in the center is the laser beam stop. The structures oriented radially from the beam stop are optical artifacts of the photographic process. Cell number AFL84.

explained the layer line intensities and fine structures observed in striated muscle diffraction patterns.

The recent development of high-resolution optical microscopy imaging techniques and the calcium tolerant single cardiac cell preparation have provided the means to directly test the basis of striated muscle diffraction theories with real structural data. Single heart cells are small enough (125 x 25 μm; see Fig. 2) so that all the sarcomeres can be transilluminated by the typical 1-mm laser beam used for diffractometry (14, 17, 19) and are also within the field of view of an high-resolution optical microscope (14, 38–41, 44). Thus, it is possible to compare actual diffraction patterns with theoretical diffraction patterns generated from a known sarcomere population obtained from these myocytes. This study aims to use the fully characterized 3-D sarcomere array data (from the accompanying paper, reference 39) to calculate Fraunhofer diffraction patterns using the numerical method of Leung (16). For these initial studies, the calculated patterns are restricted to the simplest case: a simulated pattern generated by a monochromatic laser beam normally incident upon a resting muscle. Twelve features of these calculated patterns are described and correlated with diffraction patterns obtained from resting cardiac and skeletal muscle. This numerical approach applied to a well defined muscle structure provides a more comprehensive analysis of the light diffractometry technique without assuming an idealized sarcomere periodicity and distribution.

METHODS

Isolated Heart Cell Preparation

The preparation and use of Ca^{++}-tolerant isolated heart muscle cells (Fig. 2) were described in the previous paper (39). The seven cells used in this diffraction study were selected from the preceding paper's 30-cell data set. Additional details of the cell preparation, morphology, and imaging protocols have been described previously (38, 40, 41, 44).

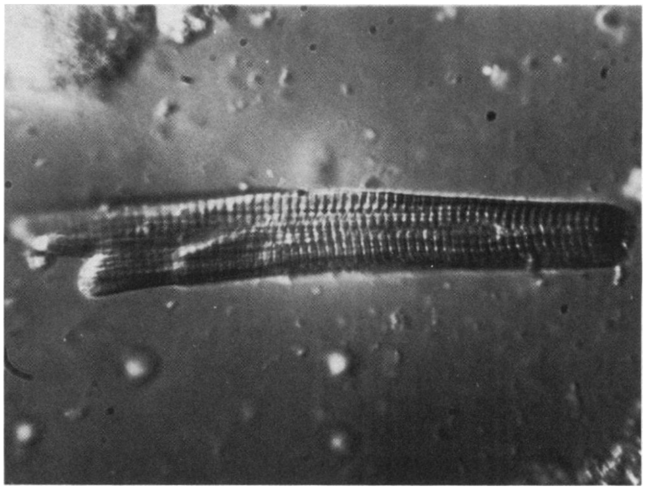

FIGURE 2 Photomicrograph of isolated heart cell. This differential interference photomicrograph illustrates a complete single heart cell with a clear striation pattern and a cell nucleus. Cell number 223.

Three-Dimensional Coordinate System

To delineate sarcomere striation pattern positions from within the cell volume and their resulting diffraction patterns when transilluminated with monochromatic light, a universal 3-D coordinate system must be defined applicable to both. Referring to Fig. 3, a single cell is assumed to

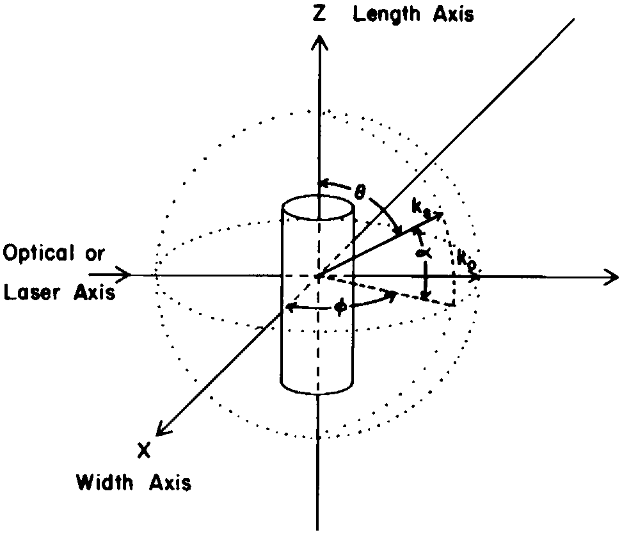

FIGURE 3 Universal 3-D coordinate system. This diagram defines the axes, coordinates, and angles used in the generation of diffraction patterns. The cylindar represents the heart muscle cell. The X (cell width), Y (cell depth, optical axis, and laser beam axis), and Z (cell length) axes are centered within this cell. Each striation's position quantified within this cell has its own x, y, and z coordinate (not shown). The diffraction pattern is determined by the $\mathbf{k}_s$ intensity vector ($\mathbf{I}[\theta, \phi]$). A complete diffraction pattern is determined from separately calculated $\mathbf{k}_s$ vectors rotated about a hemisphere (centered on the Y axis about the X–Z plane) as defined by the theta (θ) and phi (ϕ) angles. The alpha (α) angle is defined as θ–90°. See text for further explanation.

be a cylinder-like structure within which each sarcomere can be assigned an *x*, *y*, *z* position coordinate (coordinates not shown). Orienting the cell as viewed in the optical microscope, the Y axis corresponds to the optical axis of the microscope or a normally incident laser beam. Thus, changing the focus of the microscope changes the *y* coordinate. The X axis is then defined as the equatorial direction of the cell width and the Z axis as the meridional direction along the cell length. With this axis/coordinate system, sarcomere lengths are taken as the separations along a preselected line, parallel to the Z axis. The photomicrograph of Fig. 2 is an X–Z planar representation of that cell at focal plane Y.

Continuing to refer to Fig. 3, the diffraction intensity distribution on a sphere, whose center is at the intersection between the normally incident laser beam and the center of the cell can be defined by the $\mathbf{k}_s$ vector manifesting an intensity $I[\theta, \phi]$. Each individual point on the hemisphere to the right of the X–Z plane is determined by a separate $\mathbf{k}_s$ vector. The angle theta (θ) is measured from the Z (muscle fiber) axis to the $\mathbf{k}_s$ vector, and phi (ϕ) is the angle in the equatorial direction from the X (cell width) axis to the projection of the $\mathbf{k}_s$ vector on the X–Y plane. Consequently, at normal incidence, the point in hemispherical space opposite the incident beam along the Y axis is at $\theta = \phi = 90°$. The angle α in the grating Eq. 1 is $\theta - 90°$. The spacings of the layer lines are conventionally measured on the meridional plane ($\phi = 90°$) and therefore defined by either angle θ or angle α only. But the complete diffraction patterns of Figs. 1 and 5 are defined by a series of θ (or α) and ϕ angles in hemispherical space. This universal coordinate system is the same as the one used by Yeh et al. (36), and Leung (16, 22) for their theoretical analyses.

Data Acquisition

Original light diffraction patterns were obtained either from myocytes by direct photography or the scanning photomultiplier detection system (17, 19), or from previously published manuscripts by various authors studying resting cardiac and skeletal muscle (2, 3, 4–9, 12–27, 29–34, 36, 37). Simulated diffraction patterns were calculated from the striation position data obtained either from single heart cells or from model arrays.

Seven single cell data arrays were selected from the previously described uniformity study (38, 39). These data arrays have a range of resting average striation periodicities from 1.747 to 1.883 μm, at least three complete focal planes of data, and a large number of discrete sarcomere length measurements ranging from 916 to 7,496. The lateral width (*x* coordinate) steps range from 0.34 to 1.01 μm and the planar focal (*y* coordinate) steps are either 2.5 or 3.0 μm (all steps are constant within a single data set). These *x*- and *y*-step spacings provide a reasonable sample of real striation positions from each imaged cell suitable for numerically generated diffraction patterns.

Model data arrays structured similarly to those of real myocytes were also used to clarify certain diffraction pattern features. One model contained only 2.00-μm sarcomere lengths. A second model contained a normal distribution of sarcomere periodicities averaging 2.00 μm with a standard deviation of 0.176 μm. The striations of both model arrays were in register along the X and Y coordinate axes. The lateral (X) step spacing, the planar (Y) separation, the number of planes, and the overall length and width of the model arrays were varied depending on the experimental protocol. All of the cellular or modeled data arrays were stored in a computer (model PDP 11/34a or VAX model 11/730; Digital Equipment Corp, Maynard, MA) for numerical analysis with the position of each striation characterized by a unique *x*, *y*, and *z* coordinate.

Data Analysis

These 3-D striation position data were then used to calculate Fraunhofer diffraction patterns using the numerical methods, equations and computer program previously described by Leung (16). This program calculates, from all three dimensions within the cell, the magnitude of the light intensity at a point outside the cell in far-field hemispherical space defined by θ and ϕ (Fig. 3). These calculations incorporate the Ewald formalism (29–31, 37) applied to known muscle structure; Leung's Eq. 3 (17) is the same as Zite-Ferenczy's Eq. 8 (37). Each $\mathbf{k}_s$ intensity vector is calculated separately and combined graphically to form partial or complete diffraction patterns (Figs. 4 and 5). The diffraction patterns were generated as a series of calculated intensity vectors defined as a theta scan (Fig. 4), where the meridional θ was varied in 0.2° steps while the equatorial ϕ was held constant. Each theta scan required up to 30 min of CPU time on the VAX computer for computation. Surface intensity representations of diffraction patterns (Fig. 5) were generated from a series of theta scans where the ϕ was varied in steps of 1°. The intensity magnitude and centroid positions of individual meridional layer lines (e.g., the zero, first, or second orders) of a given theta scan were, respectively, calculated by integrating the area of the layer line peaks and determining their center of mass. Line widths were similarly determined from each layer line using the equations described by Kawai and Kuntz (13) and Paolini et al. (27). Diffraction pattern line widths (LW) were defined by those authors as two times the standard deviation of the sarcomere length periodicity. This calculation assumes a normal distribution of both the sarcomere periodicity and the diffraction pattern layer line. The three cells with data sets containing the largest number of discrete striation positions (exps. 135, 150, and 216) were chosen for extended analysis of their patterns. The resulting Phi scans (Figs. 6 and 7) were generated by combining the layer line intensity analyses from the individual theta scans of a complete diffraction pattern as in Fig. 5. The theta scans of Fig. 8 were generated from model data arrays.

Several reasonable assumptions have been made to use these numerical methods. First, the sarcomere is assumed to be the basic diffracting unit with light scattering mainly from the thick and thin filaments. This allows the use of the grating equation (Eq. 1) and the parameterization of the scattering. A thick filament length of 1.55 μm, a thin filament length of 1.05 μm, and a ratio between the thick and thin filament scattering amplitudes of 1:0.35 are used in these calculations; variation of these parameters can substantially effect the quantitative value of layer-line intensity, but these are based on commonly accepted values (16). Second, a homogeneous medium within the muscle is assumed. Any differences in refractive indicies or additional scattering from the cytoplasm and organelles are ignored since these structures are not periodic (they likely contribute to the background noise in real patterns, but not in the formation of the diffraction layer-lines). This assumption allows the use of Fourier transforms to calculate the Fraunhofer diffraction pattern in the far field. The Fraunhofer far-field conditions apply to all diffraction patterns from muscle when the distance between the diffractor and the detection screen is much larger than the wavelength of light. Therefore, most studies where the pattern is observed at more than ~1 cm from the specimen are in the Fraunhofer far-field region. Third, the sarcomere is assumed to be within a cylindrical myofibril of constant 1.0-μm diameter. Though this assumption better approximates skeletal rather than cardiac muscle structure, it is necessary to allow the separation of the integration variables. Fourth, the laser beam is assumed to be a plane wave. This is a reasonable approximation for single heart cell diffraction since laser beams (which have a Gaussian distribution) are usually >1,000 μm across and the source 3-D data arrays from heart cells are no more than 85 μm in length. Finally for this initial numerical study, the diffraction data generated is restricted to a monochromatic 632.8-nm laser beam at normal incidence to the cell.

RESULTS

Theta Scans

Fraunhofer diffraction patterns were calculated from the seven 3-D data arrays of heart cell striation position data obtained previously (39). Fig. 4 *a* exhibits a single meridional theta scan from a diffraction pattern where the intensity vector is calculated for θ from 40° to 140° in steps of 0.2° when the equatorial angle ϕ is held at 90° and the laser beam is at normal incidence. This theta scan from cell

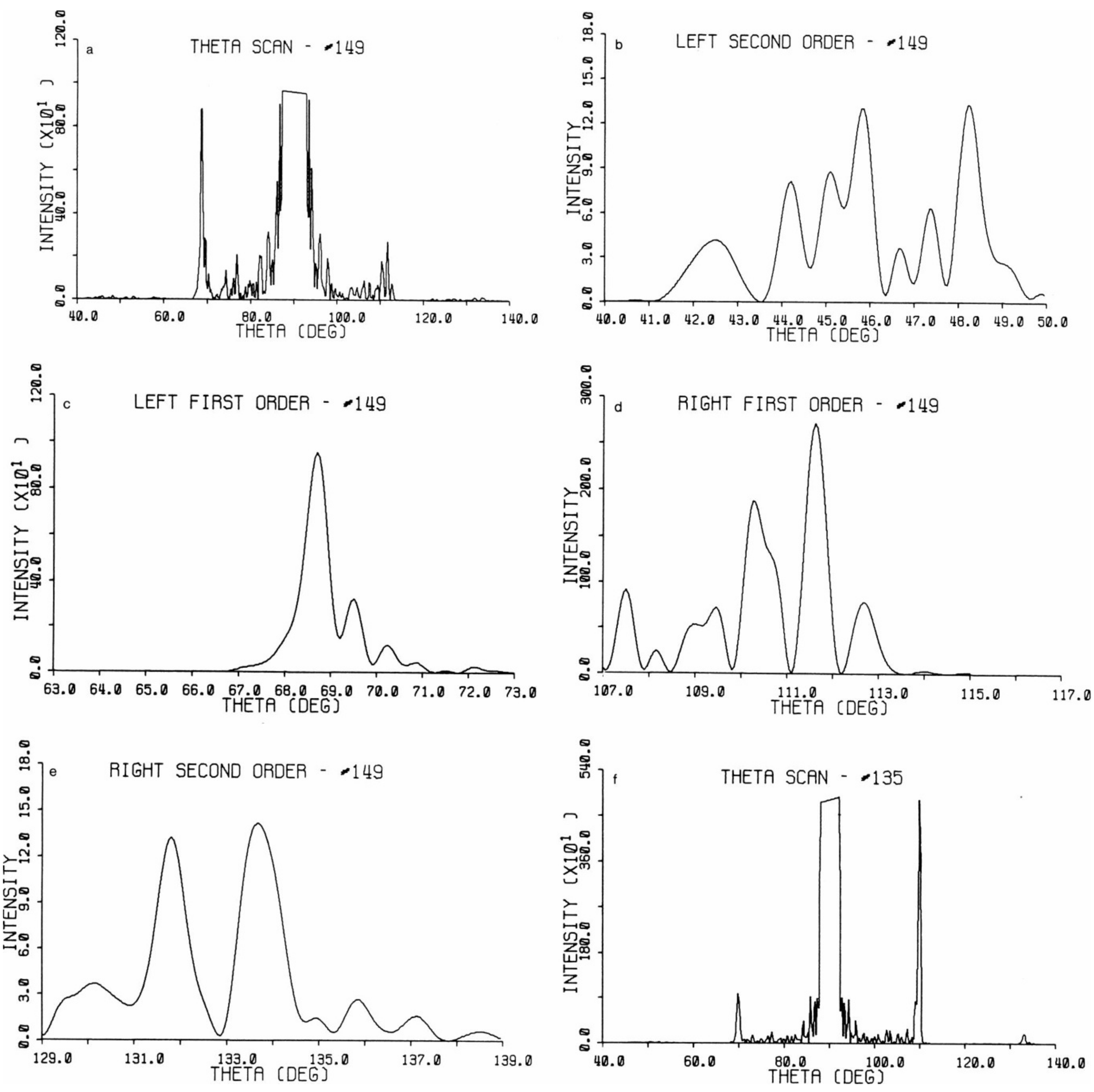

FIGURE 4 Theta scans. (*a*) Complete theta scan from $\theta = 40°$ to 140° of the zero, first, and second order meridional layer lines of cell number 149; (*b*) magnified portion of theta scan showing only the left second order of the same scan; (*c*) magnified left first order; (*d*) magnified right first order; (*e*) magnified right second order; and (*f*) complete theta scan (as in *a*) from cell number 135.

149 manifests the left second-order layer line at a calculated (θ) centroid of 45.154° ($\alpha 2L = \theta - 90° = -44.846°$), the left first-order layer line at 68.868° ($\alpha 1L = -21.132°$), the zero-order at 89.950°, the right first order at 111.278° ($\alpha 1R = 21.278°$), and the right second order at 134.226° ($\alpha 2R = 44.226°$). These four right, left, first-, and second-order layer lines are, respectively, illustrated at an enlarged scale in Fig. 4, *b–e*; the intensity scaling is different for each. Fig. 4 *f* is the meridional theta scan from cell number 135 that manifests significantly different layer-line intensities and angular positions from those of cell number 149 in Fig. 4 *a*. Since the intensity-vector calculation approaches N^2 (the square of the number of sarcomeres) at $\theta = \phi = 90°$, the zero-order intensity vectors are not calculated from θ and ϕ angles between 88° and 92°; this is a theoretical laser-beam stop.

Table I summarizes the diffraction meridional layer line angular separations, in terms of α, from the theta scans at $\phi = 90°$ for all seven cells examined. The first column is the experiment number. The second column lists the number of sarcomeres quantified within that cell's data set. The third column lists the actual average sarcomere length

TABLE I
MERIDIONAL LAYER LINE SEPARATIONS*

			First order			Second order		
			α Angle			α Angle		
Exp. No.	No. of sarcomeres	Measured SL ± SD	Expected	Observed ±LW/2	Calculated SL ± SD	Expected	Observed ±LW/2	Calculated SL ± SD
		μm	*degrees*		μm	*degrees*		μm
123	916	1.852	19.980	19.993	1.851	43.107	43.004	1.856
		0.105		0.540	0.036		11.177	0.041
135	2,158	1.847	20.036	19.924	1.857	43.253	43.117	1.852
		0.133		0.429	0.038		0.881	0.031
145	1,798	1.875	19.724	19.625	1.884	42.453	42.226	1.883
		0.138		0.336	0.031		0.909	0.033
146	1,548	1.772	20.923	21.000	1.766	45.579	45.260	1.782
		0.109		0.412	0.033		1.040	0.032
149	1,998	1.747	21.237	21.205	1.749	46.422	44.536	1.805
		0.117		0.759	0.061		0.877	0.028
150	4,096	1.850	20.002	20.081	1.843	43.166	43.083	1.853
		0.103		0.478	0.042		0.981	0.034
216	7,496	1.883	19.637	19.532	1.893	42.231	41.872	1.896
		0.105		0.407	0.038		0.791	0.029

*ϕ = 90, λ = 632.8 nm.

periodicity and its standard deviation (SD) measured directly from all the discrete striations imaged in that cell. The fourth, fifth, and sixth columns address first-order layer-line values while the seventh, eighth, and ninth columns address second-order values. The fourth and seventh columns list the angular separations (in terms of α) calculated using the grating Eq. 1 from the measured sarcomere lengths of column 3. The fifth and eighth columns list the same angle as determined from the difference between centroid positions of the calculated theta-scan layer lines divided by two (right-left/2). The angular SD in these columns is by definition ± LW/2 where LW is the calculated line width. The sixth and ninth columns are the corresponding sarcomere lengths calculated with the grating equation from the columns 5 and 8. Likewise, the length SD listed in columns 6 and 9 are calculated from the angular SD of columns 5 and 8. All data in Table I are determined from single theta scans at equatorial angle $\phi = 90°$.

Meridional Diffraction Features

These theta scan data in Table I and Fig. 4 exhibit five characteristic features seen in all the cells studied and in real diffraction patterns under the same conditions. First, the diffraction angular separation of the meridional layer lines is inversely proportional to the average sarcomere periodicity as dictated by the grating equation. For example, the shorter average sarcomere periodicities measured in cell numbers 146 and 149 have greater layer line angular separations (columns 4, 5, 7, and 8) than those of the other cells. The comparison of first-order angular separations between the two methods of calculation (column 4 vs. 5) correspond to within 0.074° on the average and 0.112° (0.6%, or 0.010 μm) in the worst case. The second-order data do not correspond nearly as well with the observed value underestimating the expected value by an average of 0.438° and the worst case exhibiting a 1.886° (4.2% or 0.057 μm) error. However, six of the seven cells are within 0.8%, nearly the same as for the first order. Despite the possible larger error in the second order, the changes in calculated angular separations do follow the grating equation in every case. (The angular separations of a given theta scan also varied with the laser beam wavelength as predicted by the grating equation.)

The second characteristic feature of diffraction patterns illustrated in Fig. 4, *a–f* is that the magnitude of the layer line intensities decrease with increasing order at the 1.74–2.00 μm sarcomere lengths used in these studies. That is, the intensity of the zero order is greater than the intensities of the first orders that are in turn greater than the intensities of the second orders. The combined right and left intensities of the second order layer lines of cell number 149 (Fig. 4, *a–e*) are only 3% of the first order at $\phi = 90°$.

The third feature is the intensity asymmetry between the right and left layer lines of both the first and second orders. In cell number 149 (Fig. 4, *a–e*), the intensity of the left ($\theta < 90°$) first-order layer line is three times larger than the corresponding right layer line; the second orders are nearly equal. For cell number 135 (Fig. 4*f*), the right first- and second-order layer lines are, respectively, 4 and 6 times larger than their corresponding left layer lines at $\phi = 90°$.

The fourth feature is the meridional angular centroid position asymmetry of the right and left layer lines of a given order about the Y (optical/laser beam) axis. The right/left α angles for a given order of layer lines for cell number 149 of Fig. 4, *a–e* (see first paragraph of this section) and for cell number 150 (see line 3 of Table II) are not equal. Other cells had asymmetries in each order of similar magnitudes.

The fifth feature, fine structure, is present within the layer lines of each order. That is, each layer line of the theta scan is usually composed of several distinct peaks whose intensities are significantly greater than the background level of scattering noise between the layer lines. These fine structure peaks may stand alone or be superimposed upon each other within the boundaries of the given layer line.

Full Diffraction Patterns

Fig. 5 illustrates a series of 61 theta scans calculated from cell number 150, where the equatorial ϕ angle has been varied from 60° to 120° to provide a surface representation of the diffraction pattern. This figure demonstrates all the previously described five features. In particular, the fine structures (feature 5) are evident in every layer line. Note that these fine structures along the layer lines are clearly defined and greater in magnitude than the interlayer line noise.

Equatorial Diffraction Features

Fig. 6, *a* and *b* plot the calculated centroid intensities of the individual right and left first-order and second-order layer lines from the same cell illustrated in Fig. 5. These phi scan data used in Fig. 6, *a* and *b* are calculated from an extended series of theta scans ranging from $\phi = 20°$ to 160°. Figs. 5 and 6 demonstrate three additional diffraction pattern features. First, as the ϕ angle is increased or decreased away from normal (90°) about the Z axis, the overall intensity magnitudes of all layer line orders tend to decrease (feature 6). Though there may be a transient increase at one equatorial step for a given layer due to fine structure fluctuations or asymmetries the overall trend is a large decrease in magnitude about $\phi = 90°$. The first-order line intensity decreases faster, but always remains greater than the second-order line-intensity magnitude. 95.6% of the diffracted light energy in the first order is contained in the layer lines between $\phi = 60°$ to 120° as illustrated in Fig. 5 (96.0% for second order). Feature 6 is similar to feature 2, but is applied in the ϕ instead of the θ orientation along the diffraction pattern.

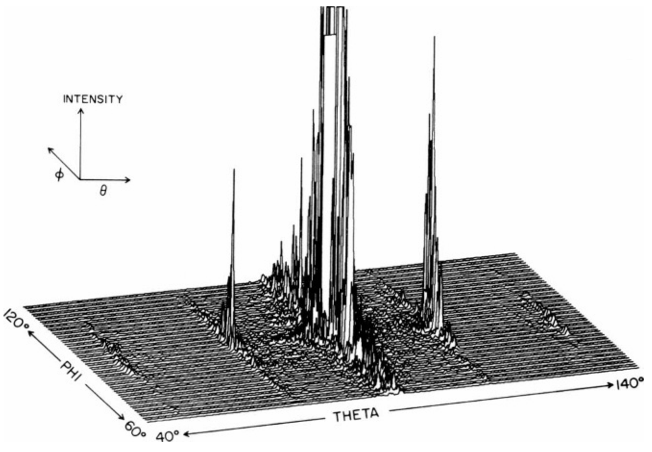

FIGURE 5 Calculated diffraction pattern. Surface plot of 61 theta scans generated from cell number 150 data. Theta varies from 40° to 140° and ϕ from 60° to 120°. The zero, first, and second order meridional layer lines are visible. The zero order is truncated at the center ($\theta = \phi = 90°$) as a theoretical laser-beam stop.

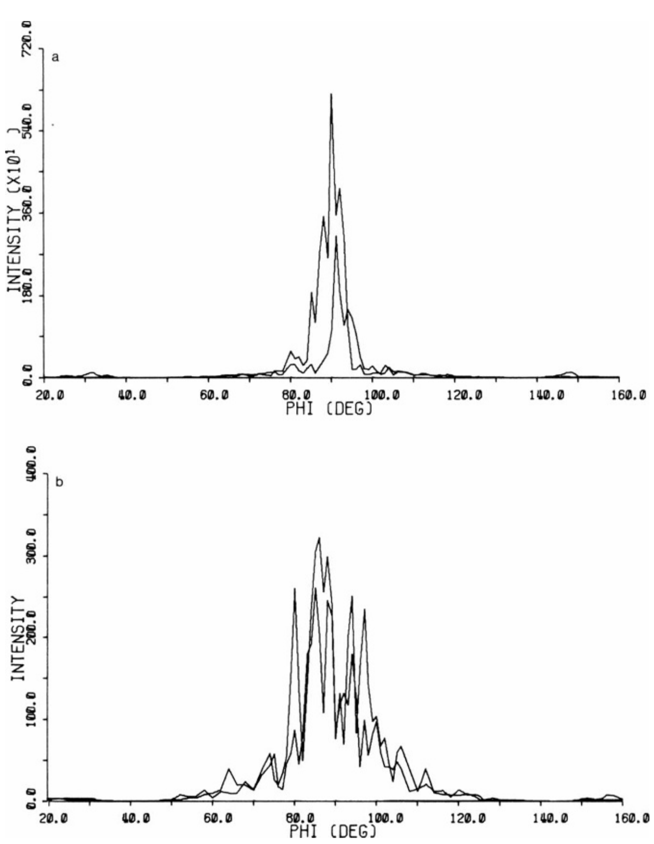

FIGURE 6 Layer-line intensity phi scan. The individual right (R1) and left (L1), *a*, first order, and *b*, second order (R2 and L2) layer-line intensities from cell number 150 are plotted as a function of equatorial ϕ from 20° to 160°.

The ϕ angular centroid of the layer line intensity may also be asymmetrical about $\phi = 90°$ (feature 7). For cell 150 in Fig. 6 *a*, the right first-order layer line exhibits its centroid of intensity at $\phi = 89.57°$ while the less intense left layer line's centroid is at $\phi = 91.86°$. Other first- and second-order layer lines also exhibited ϕ angular asymmetries, but none were greater than the 91.86° of this example. This angular asymmetry of maximum intensity feature lies in the equatorial ϕ direction as opposed to the layer line asymmetries of feature 4 that lie in the meridional θ direction.

Very small secondary equatorial intensity maxima (feature 8) are also seen at $\phi = 30.35°$ and 148.45° for the first-order phi scan of Fig. 6 *a*. These maxima contain only

~1% of the total light energy distributed within the layer lines. There are also second-order secondary maxima in Fig. 6 *b* and in the other cells examined.

These intensity phi scans of Fig. 6, *a* and *b* not only clearly show the layer line intensity decrease in the equatorial direction (feature 6) and their ϕ angular asymmetries (feature 7), but also extend the right–left layer line intensity magnitude and θ angular asymmetries previously described for single theta scans (features 3 and 4) to the entire diffraction pattern. Between $\phi = 60°–120°$, the right first-order layer line is 2.076× greater than the left's intensity for cell 150 in Fig. 6 *a*. Similarly, the other two cells examined in this way exhibited first-order layer-line intensity asymmetries of 2.117× and 1.200×. Second-order layer lines of cell number 150 (Fig. 6 *b*) exhibited some intensity asymmetry but had only 12–25% of the light energy of their corresponding first-order lines. The layer-line intensity asymmetries calculated from a single theta scan of the pattern (as in Fig. 4) are not necessarily the same as those seen in the sum of all theta scans in a diffraction pattern (as in Fig. 5) due to their individual variability.

Determination of Sarcomere Length

To examine further layer-line angular variability, Fig. 7 plots the meridional θ angular centroid positions of each layer line as measured in the equatorial (ϕ) direction from cell number 150. These data illustrate two additional features also seen in Fig. 5. The centroid position of each layer line of this angular phi scan approximate a straight line (feature 9). But there is a constant random variability in θ angular centroid position (feature 10) along each layer line. The likelihood of obtaining the exact diffraction angular separation is the same no matter where the measurement is taken along each layer line. The greater deviations seen in the second-order layer lines have already been noted in Table I at $\phi = 90°$. However, after conversion to sarcomere lengths with the grating Eq. 1, there is not really any difference between the two orders.

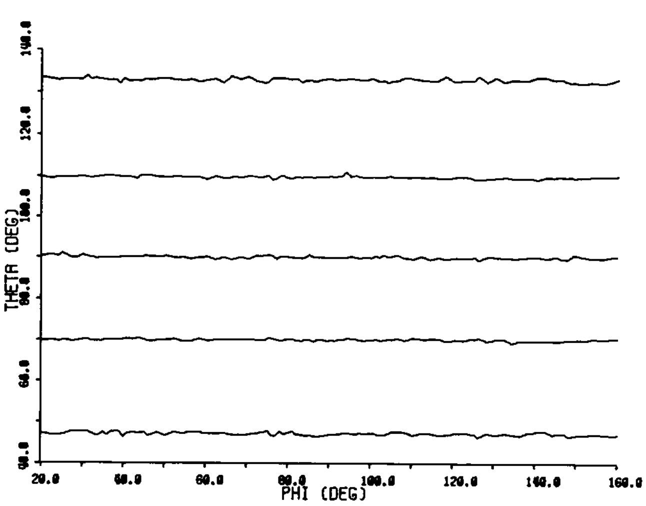

FIGURE 7 Diffraction angular separation phi scan. The θ angular positions of the zero, both first, and both second order meridional layer lines from cell number 150 are plotted as a function of the equatorial ϕ from 20° to 160°.

Table II further evaluates the meridional layer line centroid positions of cell number 150 depicted in Figs. 5 and 7. The five columns represent the five layer lines evaluated: L2, L1, 0, R1, and R2. All angular values in this table are expressed in terms of the grating equation's angle α ($\alpha = 90° - \theta$ for reference to angle θ in Figs. 5 and 7). All sarcomere length values are calculated independently with respect to an assumed zero order of $\alpha = 0°$ ($\theta = 90°$). The first line is the α angle expected (columns 4 and 7, Table I) for each order at the 1.850-µm sarcomere length measured from cell number 150. Lines 2 and 3 are the observed α angles from the $\phi = 90°$ theta scan from columns 5 and 8 of Table I and their calculated sarcomere lengths. Lines 4–7 list the observed minimum and maximum α angles and their equivalent sarcomere lengths from any theta scan

TABLE II
MERIDIONAL LAYER LINE SEPARATIONS FROM INDIVIDUAL AND AVERAGED THETA SCANS*

	L2	L1	0	R1	R2
Expected α angles at 1.850 µm	−43.166	−20.002	0.000	20.002	43.116
Observed α angles	−43.011	−20.054	−0.010	20.108	43.154
at $\phi = 90$ and calculated S.L. (in micrometers)	1.855	1.845		1.841	1.850
Observed α angles	−42.096	−19.438	−0.582	19.162	42.154
Minimum and calculated S.L. (in micrometers)	1.888	1.902		1.928	1.886
Observed α angles	−43.583	−20.376	0.581	20.251	43.847
Maximum and calculated S.L. (in micrometers)	1.836	1.818		1.828	1.827
Observed α angles ±LW/2	−42.945	−19.780	−0.023	19.894	42.916
Averaged $\phi = 60 - 120$	0.998	0.616	1.795	0.639	0.989
And calculated S.L. (in micrometers)	1.858	1.870		1.860	1.859
±SD	0.035	0.056		0.057	0.035
Averaged first order sarcomere length	1.865 µm				
Averaged second order sarcomere length	1.858 µm				

*Cell number 150, λ = 632.8 nm.

within the group of 61 illustrated in Fig. 5 ($\phi = 60°$ to 120°). Line 8 is the intensity weight averaged α angle ($\pm$L.W./2) from the sum of these 61 theta scans and line 9 is their equivalent averaged sarcomere length ($\pm$SD). Finally at the bottom of Table II in lines 10 and 11, the averaged first- and second-order sarcomere lengths are listed. As opposed to all other sarcomere length calculations in this table, these are obtained from the difference between the corresponding averaged right and left layer lines independently of the zero order (as in Table I).

These data in Table II exhibit the α angular asymmetry (feature 4) and variation (feature 10) in layer-line centroid positions from theta scan to theta scan. The sarcomere lengths calculated from the individual minimum and maximum layer line α angular separations (lines 5 and 7), ranged from 1.818 μm to 1.928 μm. The four layer-line values obtained from the sum of all 61 theta scans (line 9) are closer, but not equal to the measured value of 1.850 μm than the extreme maximum or minimum values (lines 5 and 7). These data of line 9 also illustrate that even after averaging data representing 95% of the diffraction pattern's light energy, the right and left layer-line angular separations are not symmetrical about the zero order. Finally, the sarcomere lengths calculated from the first and second orders of the averaged theta scans (lines 10 and 11) overestimate the measured sarcomere periodicity value of 1.850 μm by 0.99% and 0.62%. Other cells examined had fundamentally the same characteristics, but different specific values for layer-line intensities, angular separations, and their asymmetries.

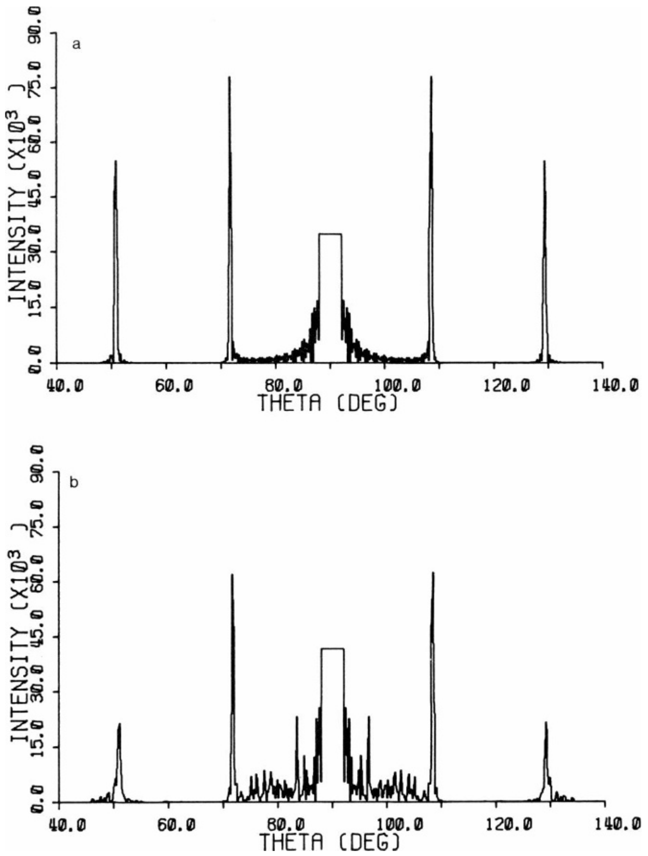

FIGURE 8 Model data array theta scans. Theta scans are calculated from triple-plane data arrays of the same size, shape, and 2.00-μm average sarcomere length periodicity. The zero deviation array used in *a* had a standard deviation of $\pm$0.00 μm while the 0.176 deviation array used in *b* had a normally distributed standard deviation of $\pm$0.176 μm.

Line Width

Finally, each layer line exhibits a characteristic spread, or line width, in the meridional (θ) direction that is primarily dependent upon the distribution of sarcomere periodicity (feature 11), and the length of the diffracting array (feature 12). The correlation between the measured sarcomere length dispersion and line width (feature 11) is not clear in these studies from the layer lines of single theta scans (comparing column 3 to either columns 6 or 9 in Table I) or from the average layer lines of 61 theta scans (lines 8 and 9 of Table II). The calculated standard deviation values based on line widths in both Tables I and II always underestimate the actual variation in the source data. To clarify this relationship, two model data arrays were constructed with the same average sarcomere length (2.00 μm) but with different standard deviations ($\pm$0.0 and $\pm$0.176 μm). These two arrays were of the exact same overall size and shape (3 different planes, 40 sarcomeres in length and 20 μm in width), and contained the same number of data points (4,680). Fig. 8, *a* and *b* illustrate the calculated diffraction pattern theta scans at $\phi = 90°$ from the zero deviation (Fig. 8 *a*) and 0.176 deviation (Fig. 8 *b*) model data arrays. The right and left layer lines of a given order are symmetrical with equal intensity and angular separation in both models; all striations in the data arrays are in register in the x–y plane. The sarcomere length determined from the layer line angular separation of both models is exactly 2.00 μm as expected. Both theta scans of Fig. 8 have sharp appearing layer lines, but those of the 0.176 deviation model theta scan have slightly wider appearing layer lines, are less intense (~11%), and exhibit considerably more interlayer line noise. The calculated line width of the zero-deviation model measures 0.526° in the first order and 0.575° in the second order. The 0.176 deviation model first-order line width measures 0.644° and the second order is 0.883° (see Table III).

Theta scans were also calculated from similar model data arrays of varying sizes, shapes and 3-D array separations. The intensities (in intensity units squared) and line widths (in degrees) calculated from modified single and multiple plane arrays of the 0.176 deviation model are listed in Table III. Lines 1 and 2 of this table demonstrate that there is no effect of the lateral separation of the data upon the intensity or line width of theta scans at $\phi = 90°$. The stacking of three planes (line 3 vs. line 1) increases the layer-line intensity, but does not alter line width. This intensity increase was not equal in that a greater proportion occurred in the second-order layer lines. Increasing or

TABLE III
MODEL ARRAY LAYER LINE INTENSITIES AND LINE WIDTHS*

Condition	Length	Width	First order Intensity	First order LW	Second order Intensity	Second order LW
	μm	*μm*	*units*^{2}	*degrees*	*units*^{2}	*degrees*
Single plane, control	80	20	12,253	0.645	2,800	0.887
Single plane, 2 × separation	80	40	12,254	0.648	2,803	0.886
3-Plane array‡, control	80	20	32,295	0.644	17,400	0.883
3-Plane array, 0.5 × width	80	10	8,079	0.651	4,349	0.877
3-Plane array, 0.5 × length	40	20	15,509	0.777	6,574	1.036
3-Plane array, 1.25 × length	100	20	38,500	0.586	21,460	0.858
3-Plane array, 2.5 × length	200	20	84,184	0.472	46,462	0.804
3-Plane array, 5 × length	400	20	197,467	0.432	76,078	0.728

*0.176 Deviation model.
‡Theta scan of this array is illustrated in Fig. 8 *b*.

decreasing the array width (line 4) also proportionally altered the layer-line intensity without changing the line widths. The main effect demonstrated in this table is that changing the length (lines 3, 5–8) of the array (by increasing or decreasing the number of sarcomeres at each end) while holding the dispersion of periodicities, array width, depth, and separations constant significantly alters the calculated line widths and intensity (feature 12). Increasing array length increased layer line intensity and decreased line width. Changes in overall data array length more strongly effect line width than changes in array dispersion of sarcomere periodicity. However, all of these size, shape, and periodicity factors may interact among themselves to confound significantly interpretation of real diffraction patterns.

DISCUSSION

General Observations

The primary finding here is that Fraunhofer diffraction patterns calculated by numerical methods (16) from real sarcomere striation pattern arrays manifest the same features as real diffraction patterns. The success of this approach affords the opportunity to compare directly the relationship between a known sarcomere array structure and its light diffraction pattern in an effort to understand their interrelationship. It is advantageous to use numerical methods to investigate this structure/pattern relationship since it is not necessary to assume any restrictions on distribution, ordering or orientation of the muscle's diffracting structures. It does not matter whether there are domains of uniform sarcomere lengths, Bragg, or skew planes of striation registration, or any other structural ordering. These numerical methods are structure-independent in that they calculate the diffraction pattern from every diffraction scattering point in full 3-D relationship to every other scattering point within the source data array. Despite several mathematical assumptions (see Methods) and the study's restriction to resting cells at normal laser beam incidence, the calculated data correlates well to observed diffraction phenomenon that further supports this new 3-D numerical method approach as an appropriate and effective means to evaluate diffraction patterns.

Note that the isolated heart muscle cell preparation is a nearly ideal preparation to provide a basis for this comparative study. From the viewpoint of striation pattern imaging, the cell is small enough to be able to quantify nearly all the sarcomeres. Heart cell striations are generally in register (though often skewed or disrupted in a noncrystalline scheme) and their sarcomere length periodicities appear to be distributed normally throughout most of the cell volume (39). From the viewpoint of light diffractometry, the single heart cell has two advantages over larger cardiac or skeletal muscle preparations. First, the entire cell is within the laser beam eliminating any ambiguity concerning the number of sarcomeres or the portion of muscle examined during the experiment. Second, it is a relatively thin preparation that has proved advantageous for precision diffractometry of skeletal muscle fibers (23). Though all of the calculated diffraction patterns were obtained only from isolated heart cell or similar model sarcomere position data arrays, the general characteristics of their calculated diffraction patterns are comparable to real patterns not only from single heart cells, but also from multicellular cardiac and skeletal muscle preparations. Questions involving specific structural relationships to diffractometry in skeletal muscle fibers such as domains, tilt angles, and near-field fine structures may have to await further direct data imaging and analyses of that preparation (4, 9, 12, 18, 22, 23, 30, 32, 33, 35, 37).

Several of the 12 features observed in both the real and simulated diffraction patterns (Figs. 4–8) are fundamental characteristics of diffraction manifested in the grating equation and its boundary conditions within a muscle. These include the inverse relationship between the sarcomere periodicity and meridional layer line separation (feature 1), the layer-line intensity decrease in both the meridional and equatorial directions about the laser beam (features 2 and 6), secondary equatorial maxima (feature 8), and the overall linearity of meridional layer-line angular (θ or α) separation at any ϕ angle on the hemispherical surface (feature 9). These fundamental features of muscle light diffractometry have long been described and illustrated in the literature (2–9, 12–23, 25–29, 33, 34, 36, 42).

Secondary Equatorial Maxima

An additional comment is in order regarding the small secondary equatorial intensity maxima along each layer line (feature 8, Fig. 6). For these numerically derived diffraction patterns, they are likely artifactual in nature arising from the fixed lateral (x direction) spacing of the theta scans in the data array used in the calculation. For cell number 150 used in Fig. 6, the sarcomere length is 1.850 μm and the data acquisition lateral step spacing (x_0) is 0.82 μm. Applying the grating Eq. 1 in the equatorial direction, a secondary ϕ angular maxima of the first order (ϕ_1) can be estimated from the following approximation:

$$\phi_n = \cos^{-1} n\lambda / x_0 \sin \theta_n. \tag{2}$$

Therefore ϕ_1 is estimated to be 34.8° and observed at a reasonably close 31.0°. The secondary maxima seen in real skeletal muscle patterns are due to the diffraction from a bundle of myofibrils of similar diameters (20, 21). It is difficult for investigators to observe equatorial secondary maxima in real single-heart-cell diffraction patterns since the overall layer-line intensity magnitudes are very small except near $\phi = 90°$. Furthermore, the lack of well defined myofibrils in cardiac muscle makes the likelihood of the appearance of secondary maxima very small under any conditions.

Diffraction Asymmetries

Of greater interest to investigators using the light diffraction technique to monitor average sarcomere periodicity are the layer-line intensity and angular asymmetry, fine structure, and line width features. It is important to understand what effect (if any) these features might have in the interpretation of observed diffraction phenomenon. Though complete resolution of all questions of this nature is not possible within the scope of this study, these calculated diffraction patterns correlated to known structure can provide some new understanding into these critical features.

The diffracted light intensity and angular asymmetries in both the meridional and equatorial directions (features 3, 4, and 7) have been described in the literature (2, 4, 9, 17, 18, 22–24, 29–31, 37) for both skeletal and cardiac muscle diffraction patterns. The right–left layer-line intensity asymmetry (feature 3) was seen in six of the seven calculated diffraction patterns, while their corresponding θ angular separation asymmetry about the zero order (feature 4) was seen in all seven cells. The ϕ angular asymmetry of the layer-line intensity in the equatorial direction (feature 7) was seen (Figs. 5 and 6) in all three cells examined comprehensively. These asymmetries at normal incidence have been widely discussed in the literature by Baskin et al. (2), Fujime (8), Gilliar et al. (9), Leung (17, 22), Lieber et al. (23), and Rudel and Zite-Ferenczy (29–31, 37). Though these studies disagree on the exact structural ordering necessary to produce these asymmetries, they all hypothesize that there is some sort of structural imperfection (be it Bragg planes, skew planes, or random packing) sensitive to the direction of the incident light.

Diffraction patterns calculated by numerical methods from both model data arrays of in register multiple planes (Fig. 8) have no intensity and angular asymmetries. Diffraction patterns calculated from single planes of cell data demonstrated the same symmetric features as the model arrays. These findings of both meridional and equatorial asymmetries (features 3, 4, and 7) from cell data arrays along with their disappearance in single plane or in multiple plane arrays with perfect registration, reinforce the three dimensionality of the diffraction process and its sensitivity to structural organization. This is direct evidence that sarcomeric ordering is responsible for these types of asymmetries. Therefore, it is logical that the structural skewing and misregistration of varying degrees found in both the meridional and equatorial directions of cell data arrays contribute to the process of diffraction pattern formation. Also, recent preliminary studies (43) extending this current theoretical work to variable incident angles (ω) and cell rotations about the Z axis (similar to Gilliar et al., reference 9) indicate that the intensity and angular asymmetries seen at normal incidence directly correspond to the magnitude of array misregistration.

Fine Structure

Another important diffractometric feature is the fine structure (feature 5). It is observed in all orders of every theta scan anywhere in the hemispherical space of the diffraction pattern calculated from cell data arrays. The specific intensity and the exact positions of the fine structures differ in different cells. There appears to be no generalized spacing between fine structures from one cell to the next in either the θ or ϕ directions. The fine structure itself must arise from the interaction of the individual sarcomere periodicities and their specific ordering in the muscle cell, since each of the source cell data arrays were unique. Fine structures were not evident in single-plane-cell theta scans, in the zero deviation model array theta scan of Fig. 8 *a*, nor in data summed from all theta scans of the diffraction pattern used to calculate lines 8 and 9 of Table II. Furthermore, the fine structures do not necessarily arise from a regional domain of essentially identical sarcomere lengths (4, 32, 35) since this does not seem to exist in isolated heart cells (39). Any direct correlation of specific sarcomeres and fine structures must be done on the same cell. It has not yet been technically feasible to three-dimensionally image and diffractometrically examine the same cell for this type of direct comparison. A complete analysis of the source and characteristics of diffraction fine structures has been recently detailed by Leung (22).

Fine structure variation from theta scan to theta scan within a single diffraction pattern can elicit very different apparent layer line angular separations as demonstrated in lines 4–7 of Table II and the jitter in each layer line centroid position along the ϕ angle in Fig. 7 (feature 10). The exact diffraction angular separation of the layer line is dependent upon the volumetric interference relationship that generates the fine structures. The calculated sarcomere lengths from averaged data (lines 8 and 9 of Table II) are considerably more accurate than the sarcomere lengths calculated from a single theta scan. The maximum/minimum values the first-order layer lines of cell number 150 from Table II vary by 0.110 μm or by 6.1%. An intensity fluctuation in a single fine structure resulting from some volumetric interference at a given $\mathbf{k}_s$ intensity vector $[\theta, \phi]$ can significantly alter the calculated centroid position of a layer line at that point in the hemispherical space. Consequently, the θ angular position of the layer line centroid varies randomly with ϕ as seen in Fig. 7. This centroid jitter is especially critical with the second-order layer lines where the intensity magnitude can be very low in heart cells and the calculation influenced by the background interlayer-line scattering noise. An exact correlation between measured periodicities and layer-line spacing (as in Tables I and II) would only be expected if the entire diffraction pattern were to be evaluated from a muscle exhibiting perfectly aligned structures in a homogeneous medium (i.e., no other membranes, organelles, and so on). Only then would there be no contributions from fine structures or 3-D structural ordering.

There is also inter-layer line noise present in both the real (Fig. 1) and calculated (Fig. 5) diffraction patterns. The source of this noise has not been specifically identified, but it is always distinguishable from the layer lines themselves and their associated fine structures. The model array studies of Fig. 8 suggest that this noise most likely arises from higher-order 3-D interference between diffracting structures since the noise is very low and highly ordered in the zero deviation model pattern of Fig. 8 *a*. It is much greater and less ordered in the randomized model of Fig. 8 *b*. The noise between the zero and first orders is greater than the noise between the first and second orders. This is responsible for the slight underestimation of diffraction angle (and therefore the overestimation of calculated sarcomere length) in Tables I and II, especially in the second order where the noise is proportionally greater relative to their layer-line intensities. This systematic error may also occur in measurements from real diffraction patterns since they also demonstrate interlayer-line noise. Additional interlayer-line noise is probably present in real diffraction patterns because the nonperiodic scatterers such as mitochondria and nuclei contribute to a more heterogenous pattern formation.

Line Widths

Finally, the line widths (features 11 and 12) determined from calculated diffraction patterns of cellular (Tables I and II) and model (Fig. 8 and Table III) sarcomere arrays do not quantitatively correlate to the actual distribution of sarcomere lengths when the traditional mathematical expressions are used (13, 27). The calculated values from cell data arrays tend to underestimate the actual sarcomere length standard deviation by twofold to threefold, and do not appear to reflect the actual increases or decreases in measured sarcomere length dispersion from single theta scans of different cells in Table I. These results are not surprising because diffraction line width depends on factors other than sarcomere length dispersion such as the length of the sarcomere array, the wavelength of diffracting light, superimposed noise from nonperiodic scatters and other volumetric interference phenomenon. In addition, the equations used to calculate line width suffer from two serious flaws: they are highly intensity-dependent and they assume a Gaussian (normal) shaped layer line, ignoring the contribution of fine structures. All of these factors confound the interpretation of line widths from real and calculated diffraction patterns. Thus, the mathematical expressions traditionally used to calculate the diffraction layer line line width (13, 27) should not be expected to reflect the actual dispersion of sarcomere length or any other single parameter.

Despite the ambiguity of the line width calculation, changes in sarcomere length dispersion do positively correlate to measured line widths (feature 11) under the rigidly controlled modeling conditions of Fig. 8. The increases and decreases seen are small, but real. The line widths measured from the patterns of model arrays are of the same order than those from similarly sized cell arrays. The greater heterogeneity (mitochondrial gaps and nuclear holes) of the cell arrays likely contribute to their greater variability in line widths and interlayer-line noise.

Layer-line intensities and line widths are more significantly altered by changes in model data array length (feature 12, Table III). This is additionally confounded by all the other 3-D interference and the diffraction process itself. In general, as the cell becomes shorter (theoretically equal to a smaller laser beam diameter), the layer-line intensity decreases and the line width increases; as the cell becomes longer (theoretically equal to a larger laser beam diameter), the intensity increases and the line width decreases. This effect is primarily due to the diffraction process itself. At short cell lengths, the diffraction is less like an infinite grating and more like a single slit in nature; therefore the line width increases. At longer cell lengths, diffraction behaves more like an infinite grating than a single slit and the line width decreases. (There are measurable line widths from even the zero deviation model patterns because the data arrays are not infinitely long.) The layer line intensity is merely a direct function of the number of diffracting elements and the number of planes; increasing the number of data planes tend to increase higher-order layer-line intensities relative to their lower orders as seen in Table III. Even this length effect is often obscured by other 3-D interference effects in cell data that can transiently modify a given layer line's intensity and line width. Overall, cell length (or beam diameter) is the most important parameter in the determination of line widths. Therefore, it is not surprising that there is no apparent correlation of line widths to sarcomere length dispersion in Table I, where the cell data arrays have different number of planes, number of data points, lengths, and fine structure interferences. Taken as a whole, these data suggest that caution should be applied to the interpretation of diffraction pattern line widths and dispersions from real diffraction patterns. However, under controlled conditions, dynamic changes in line width may provide valuable inferences about sarcomere length dispersion.

Technical Suggestions

Several recent studies using skeletal muscle have directly and indirectly raised the question of precision and reliability of the technique in relation to sarcomere striation orientation, translation and dynamics (1, 4, 5, 9, 11, 12, 18, 22–24, 28–33, 35, 36). Although it is not possible to address directly these questions from this limited study, its results suggest several approaches already used by many investigators to reduce any measurement error due to asymmetries or fine structures. First, the diffraction angular separation used in the sarcomere length calculation should only be determined from both the right and left layer lines of a given order as in Table I or lines 10 and 11 of Table II. Second, more than one order of layer-line pairs should be examined if possible. And third, the entire meridional layer line should be used through a full range of ϕ to average out the random fine structures present instead of just a single representative theta scan. For most investigators, this will mean the use of a cylindrical or hemispherical (not flat) screen for pattern detection in order not to introduce geometrical error at large ϕ angles (27, 37). All of these suggestions are based on the fact that the entire hemisphere of the diffraction pattern contains structural information about the periodicity. Therefore, measurement of only a portion of the pattern may bias the data. No doubt, there will still be some volumetric interference effects that can induce systematic error in average sarcomere length determination, but these will be considerably reduced if the above suggestions are employed.

In conclusion, Fraunhofer diffraction patterns have been calculated from discrete sarcomere arrays of resting isolated heart muscle cells with numerical methods. Calculated patterns exhibit the same features observed in real resting striated muscle diffraction patterns at normal laser beam incidence. It has been shown that diffractometric sarcomere length determination can now be directly evaluated by comparison of actual sarcomere measurements and their corresponding calculated diffraction patterns. These data confirm that theoretical calculations can predict real muscle diffraction patterns and their asymmetries.

The authors wish to thank Drs. Allan J. Brady and Richard L. Lieber for their reviews of this manuscript. We would also like to thank Bradford A. Lubell for his assistance in the software development and Dr. Richard Horn for hundreds of hours of CPU time on his VAX to crunch all the numbers. The technical assistance of Cecelia Duenas, Barbara Erickson, and Andy Fukudome was invaluable in the preparation of the heart cells, and data processing.

This work was supported by U.S. Public Health Service grant HL29671, American Heart Association, Greater Los Angeles Affiliate grant 695-G1-3, and the Laubisch Endowment to K. P. Roos; additional support was obtained from U.S. Public Health Service grant HL30828 to Allan J. Brady.

Received for publication 6 May 1985 and in final form 6 February 1987.

REFERENCES

1. Altringham, J. D., R. Bottinelli, and J. W. Lacktis. 1984. Is stepwise shortening an artifact? *Nature (Lond.).* 307:653–655.
2. Baskin, R. J., R. L. Lieber, T. Oba, and Y. Yeh. 1981. Intensity of light diffraction from striated muscle as a function of incident angle. *Biophys. J.* 36:759–773.
3. Baskin, R. J., K. P. Roos, and Y. Yeh. 1979. Light diffraction study of single skeletal muscle fibers. *Biophys. J.* 28:45–64.
4. Brenner, B. 1985. Sarcomeric domain organization within single skinned rabbit psoas fibers and its effects on laser light diffraction patterns. *Biophys. J.* 48:967–982.
5. Cleworth, D. R., and K. A. P. Edman. 1972. Changes in sarcomere length during isometric tension development in frog skeletal muscle. *J. Physiol. (Lond.).* 227:1–17.
6. Fujime, S. 1975. Optical diffraction study of muscle fibers. *Biochim. Biophys. Acta.* 379:227–238.
7. Fujime, S., and S. Yoshino. 1978. Optical diffraction study of muscle fibers. I. A theoretical basis. *Biophys. Chem.* 8:305–315.
8. Fujime, S. 1984. An intensity expression of optical diffraction from striated muscle fibers. *J. Muscle Res. Cell. Motil.* 5:577–587.
9. Gilliar, W. G., W. S. Bickel, and W. F. Bailey. 1984. Light diffraction studies of single fibers as a function of fiber rotation. *Biophys. J.* 45:1159–1165.
10. Ishiwata, S., K. Muramatsu, and H. Higuchi. 1985. Disassembly from both ends of thick filaments in rabbit skeletal muscle fibers. An optical diffraction study. *Biophys J.* 47:257–266.
11. Jacobson, R. C., R. Tirosh, M. J. Delay, and G. H. Pollack. 1983. Quantatized nature of sarcomere shortening steps. *J. Muscle Res. Cell Motil.* 4:529–542.
12. Judy, M. M., V. Summerour, T. LeConey, R. L. Roa, and G. H. Templeton. 1982. Muscle diffraction theory. Relationship between diffraction subpeaks and discrete sarcomere length distributions. *Biophys. J.* 37:475–487.
13. Kawai, M., and I. D. Kuntz. 1973. Optical diffraction studies of muscle fibers. *Biophys. J.* 13:857–876.

14. Krueger, J. W., D. Forletti, and B. A. Wittenberg. 1980. Uniform sarcomere shortening behavior in isolated cardiac muscle cells. *J. Gen. Physiol.* 76:587–607.
15. Krueger, J. W., and G. H. Pollack. 1975. Myocardial sarcomere dynamics during isometric contraction. *J. Physiol. (Lond.).* 251:627–643.
16. Leung, A. F. 1982*a*. Calculation of the laser diffraction intensity of striated muscle by numerical methods. *Comput. Programs Biomed.* 15:169–174.
17. Leung, A. F. 1982*b*. Laser diffraction of single intact cardiac muscle cells at rest. *J. Muscle Res. Cell Motil.* 3:399–418.
18. Leung, A. F. 1983*a*. Light diffractometry for determining the sarcomere length of striated muscle: an evaluation. *J. Muscle Res. Cell Motil.* 4:473–484.
19. Leung, A. F. 1983*b*. Sarcomere dynamics in single myocardial cells as revealed by high-resolution light diffractometry. *J. Muscle Res. Cell Motil.* 4:485–502.
20. Leung, A. F. 1983*c*. Light diffraction by striated muscle fibers in the transverse direction. *J. Muscle Res. Cell Motil.* 4:557–568.
21. Leung, A. F., J. C. Hwang, and Y. M. Cheung. 1983. Determination of myofibrillar diameter by light diffractometry. *Pfluegers Arch. Eur. J. Physiol.* 396:238–242.
22. Leung, A. F. 1984. Fine structures in the light diffraction pattern of striated muscle. *J. Muscle Res. Cell Motil.* 5:535–558.
23. Lieber, R. L., Y. Yeh, and R. J. Baskin. 1984. Sarcomere length determination using laser diffraction: the effect of beam and fiber diameter. *Biophys. J.* 45:1007–1016.
24. Morgan D. L. 1978. Predictions of some effects on light diffraction patterns of muscles produced by areas with different sarcomere lengths. *Biophys. J.* 21(2, Pt. 2):88a. (Abstr.)
25. Nassar, R., A. Manring, and E. A. Johnson. 1974. Light diffraction of cardiac muscle sarcomere motion during contraction. *In* The Physiological Basis of Starling's Law of the Heart. Elsevier/North Holland, Amsterdam. 57–91.
26. Paolini, P. J., K. P. Roos, and R. J. Baskin. 1977. Light diffraction studies of sarcomere dynamics in single skeletal muscle fibers. *Biophys. J.* 20:221–232.
27. Paolini, P. J., R. Sabbadini, K. P. Roos, and R. J. Baskin. 1976. Sarcomere length dispersion in single skeletal muscle fibers and fiber bundles. *Biophys. J.* 16:919–930.
28. Pollack, G. H., T. Iwazumi, H. E. D. J. ter Keurs, and E. F. Shibata. 1977. Sarcomere shortening in striated muscle occurs in stepwise fashion. *Nature (Lond.).* 268:757–759.
29. Rudel, R., and F. Zite-Ferenczy. 1979a. Do laser diffraction studies on striated muscle indicate stepwise sarcomere shortening? *Nature (Lond.).* 278:573–575.
30. Rudel, R., and F. Zite-Ferenczy. 1979b. Interpretation of light diffraction by cross-striated muscle as Bragg reflexion of light by the lattice of contractile proteins. *J. Physiol. (Lond.).* 290:317–330.
31. Rudel, R., and F. Zite-Ferenczy. 1980. Efficiency of light diffraction by cross-striated muscle fibers under stretch and during isometric contraction. *Biophys. J.* 30:507–516.
32. Sundell, C. L., Y. E. Goldman, and L. D. Peachey. 1986. Fine structure in near-field and far-field laser diffraction patterns from skeletal muscle fibers. *Biophys. J.* 49:521–530.
33. Tameyasu, T., N. Ishide, and G. H. Pollack. 1982. Discrete sarcomere length distribution in skeletal muscle. *Biophys. J.* 37:489–492.
34. Umazume, Y., and S. Fujime. 1975. Electro-optical property of extremely stretched skinned muscle fibers. *Biophys. J.* 15:163–180.
35. Williams, W. J. 1984. 3-D computer reconstruction of single skeletal muscle fibers. *Biophys. J.* 45(2, Pt. 2):103a. (Abstr.)
36. Yeh, Y., R. J. Baskin, R. L. Lieber, and K. P. Roos. 1980. Theory of light diffraction by single skeketal muscle fibers. *Biophys. J.* 29:509–522.
37. Zite-Ferenczy, F., K. D. Haberle, R. Rudel, and W. Wilke. 1986. Correlation between the light diffraction pattern and the structure of a muscle fibre realized with Ewald's construction. *J. Muscle Res. Cell Motil.* 7:197–214.
38. Roos, K. P. 1986. Three dimensional reconstructions of optically imaged single heart cell striation patterns. *Biophys. J.* 49:44–46.
39. Roos, K. P. 1987. Sarcomere length uniformity determined from three dimensional reconstructions of resting isolated heart cell striation patterns. *Biophys. J.* 52:317–327.
40. Roos, K. P., and A. J. Brady. 1982. Individual sarcomere length determination from isolated cardiac cells using high-resolution optical microscopy and digital image processing. *Biophys. J.* 40:233–244.
41. Roos, K. P., A. J. Brady, and S. T. Tan. 1982. Direct measurement of sarcomere length from isolated cardiac cells. *Am. J. Physiol.* 242:H68–H78.
42. Ranvier, L. 1874. Du spectre produit par les muscles stries. *Arch. Physiol. Norm. Path.* 6:775–780.
43. Roos, K. P., and A. F. Leung. 1985. Theoretical Fraunhofer light diffraction pattern omega scans calculated from real and modified striated muscle 3-D sarcomere assays. *Biophys. J.* 47(2, Pt. 2):125a. (Abstr.)
44. Brady, A. J., S. T. Tan, and N. V. Ricchiuti. 1979. Contractile force measured in unskinned adult rat heart fibers. *Nature (Lond.).* 282:728–729.